



## Numerical simulation of tsunami-scale wave boundary layers

Williams, Isaac A.; Fuhrman, David R.

*Published in:*  
Coastal Engineering

*Link to article, DOI:*  
[10.1016/j.coastaleng.2015.12.002](https://doi.org/10.1016/j.coastaleng.2015.12.002)

*Publication date:*  
2016

*Document Version*  
Peer reviewed version

[Link back to DTU Orbit](#)

*Citation (APA):*  
Williams, I. A., & Fuhrman, D. R. (2016). Numerical simulation of tsunami-scale wave boundary layers. *Coastal Engineering*, 110, 17-31. <https://doi.org/10.1016/j.coastaleng.2015.12.002>

---

### General rights

Copyright and moral rights for the publications made accessible in the public portal are retained by the authors and/or other copyright owners and it is a condition of accessing publications that users recognise and abide by the legal requirements associated with these rights.

- Users may download and print one copy of any publication from the public portal for the purpose of private study or research.
- You may not further distribute the material or use it for any profit-making activity or commercial gain
- You may freely distribute the URL identifying the publication in the public portal

If you believe that this document breaches copyright please contact us providing details, and we will remove access to the work immediately and investigate your claim.

# Numerical simulation of tsunami-scale wave boundary layers

Isaac A. Williams<sup>a,b</sup>, David R. Fuhrman<sup>c,\*</sup>

<sup>a</sup>*Department of Physical Geography, Utrecht University, 3508 TC Utrecht, The Netherlands*

<sup>b</sup>*Current address: University of Twente, Faculty of Engineering Technology, Department of Water Engineering & Management, P.O. Box 217, 7500 AE Enschede, The Netherlands*

<sup>c</sup>*Technical University of Denmark, Department of Mechanical Engineering, DK-2800 Kgs. Lyngby, Denmark*

---

## Abstract

This paper presents a numerical study of the boundary layer flow and properties induced by tsunami-scale waves. For this purpose, an existing one-dimensional vertical (1DV) boundary layer model, based on the horizontal component of the incompressible Reynolds-averaged Navier-Stokes (RANS) equations, is newly extended to incorporate a transitional variant of the standard two-equation  $k-\omega$  turbulence closure. The developed numerical model is successfully validated against recent experimental measurements involving transient solitary wave boundary layers as well as for oscillatory flows, collectively demonstrating the ability to reproduce accurate velocity profiles, turbulence, and bed shear stresses on both smooth and rough beds. The validated model is then employed for the study of transient wave boundary layers at full tsunami scales, covering a wide and realistic geophysical range in terms of the flow duration, bottom roughness, and associated Reynolds numbers. For this purpose, three different “synthetic” (idealised) tsunami wave descriptions are considered i.e. invoking: (1) single wave (solitary-like, but with independent period and wave height), (2) sinusoidal, and (3) N-wave descriptions. The flow, boundary layer thickness, turbulence, and bed shear stresses induced are systematically monitored and parameterised, under both hydraulically smooth and rough bed conditions. The results generally support a notion that the boundary layers induced by

---

\*Corresponding author

Email addresses: [i.a.williams@utwente.nl](mailto:i.a.williams@utwente.nl) (Isaac A. Williams ), [drf@mek.dtu.dk](mailto:drf@mek.dtu.dk) (David R. Fuhrman )

tsunami-scale waves are both current-like, due to their long durations, but also wave-like in the sense that the boundary layer will not necessarily span the entirety of the water column. The results likewise suggest that there is a continuum connecting wind-wave and tsunami-wave scales, as existing expressions commonly used for characterising boundary layer properties beneath wind waves maintain reasonable accuracy when extrapolated to full tsunami scales. Boundary layers driven by actual field-measured tsunami signals are likewise simulated, stemming from both the 2004 Indian Ocean as well as the 2011 Tohoku events. These results are reconciled with the various synthetic tsunami signals considered, generally confirming their usefulness as idealised tsunami waves.

*Keywords:* Tsunami, boundary layer, turbulence, laminar-to-turbulence transition,  $k$ - $\omega$  model

---

## 1. Introduction

The detailed understanding of wave and/or current boundary layer processes is essential for the quantitative assessment of near-bed flow velocities, associated turbulence, and the prediction of bed shear stresses in coastal and offshore regions. These in turn form the basis for subsequent predictions involving e.g. sediment transport and morphology, scour around coastal and offshore structures, or settled contaminant transport and diffusion in marine environments. This general importance holds for the full array of boundary layer-inducing flows in oceanic regions, ranging from relatively short-scale wind waves (periods typically 5–15 s) to much longer tidal currents (periods of approximately 12 h). Due to their extreme lengths such tidal currents can be reasonably treated as momentarily steady for many practical purposes. Alternatively, due to their relatively short periods, the bottom boundary layers induced by wind waves can be effectively reproduced experimentally at full scale within oscillatory tunnel environments (Jensen et al., 1989), and have therefore been extensively studied in the literature. Lying in between these extremes are infrequent, but potentially devastating and dramatic, tsunami wave events, which are characterised by periods (ranging from several minutes to hours) and/or flow velocities that can be well in excess of typical wind-wave scales. Due to their long, yet unsteady and transient nature, tsunami scales are difficult, if not impossible, to achieve in controlled laboratory settings. As a result, the boundary layer dynamics beneath full tsunami-scale waves has received little specific attention in the literature.

The general topic of transient wave boundary layer dynamics, on the

other hand, has received considerable attention in recent years. Most commonly studies have focused on the boundary layer developing beneath idealised solitary waves. Theoretical solutions for laminar boundary layer flow have been derived by Liu et al. (2007), whilst the experimental work of Sumer et al. (2010, 2011) has provided a quantitative insight into the boundary layer dynamics across the transition from laminar to fully turbulent conditions. Though direct numerical simulations have proved capable of providing a detailed description of the experimentally observed flow field across these scales (Vittori and Blondeaux, 2008, 2011), they are computationally intensive and thus unsuitable for practical engineering applications. For these purposes turbulence models based on the Reynolds-averaged Navier-Stokes equations are more appropriate. Such models, which have been successful in suitably describing the flow and turbulence structure for boundary layers under oscillatory waves (e.g. Blondeaux, 1987; Blondeaux et al., 2012), have recently been applied to the study boundary layer dynamics beneath solitary waves. For example, Suntoyo and Tanaka (2009), who used the closure of Menter (1994), found results that were, at least, qualitatively consistent with the experimental work of Sumer et al. (2010). More recently Blondeaux and Vittori (2012) used the closure of Saffman (1970) to directly simulate experimental cases of Sumer et al. (2010). The computed boundary layer flow compared favourably with the experimental measurements, with the model adequately detailing the transition from laminar to turbulent conditions.

The preceding discussion is pertinent to tsunamis as solitary waves represent a traditional paradigm in tsunami research (e.g. Synolakis, 1986, 1987; Yeh et al., 1994). However, the aforementioned theoretical, experimental and numerical works examining boundary layer dynamics beneath solitary waves do not approach the extremely long flow durations and large Reynolds numbers expected beneath actual tsunami waves (see e.g. the discussion of Madsen et al., 2008). Further, in spite of the frequent use of solitary waves in tsunami studies their relevance to real-world geophysical tsunamis has been questioned (e.g. Madsen et al., 2008; Chan and Liu, 2012). The lack of field-measurements corresponding to real-world tsunamis has, in part, hindered the assessment of their validity.

By means of a numerical study, the present work aims to examine boundary layer flow at realistic geophysical tsunami scales and to explore the relevance that idealised signals, e.g. that of solitary-like waves, hold for actual field-measured tsunamis. For this purpose an existing one-dimensional vertical (1DV) numerical model for simulating turbulent boundary layer flows will be utilised (Fuhrman et al., 2013), newly extended to incorporate a

transitional two-equation  $k-\omega$  turbulence closure.

The remainder of this paper is organised as follows: The governing equations and numerical model are first presented in Section 2. In Section 3 the model will then be validated, largely for transient solitary-type waves based on the experimental measurements of Sumer et al. (2010). In Section 4 the model will be utilised for the simulation of tsunami-scale wave boundary layers based on three idealised synthetic wave forms, characterised as: (1) single (i.e. solitary-like, but with independent wave height and period), (2) sinusoidal, and (3) N-waves. The flow velocities, turbulence, and bed shear stresses will be systematically monitored and parameterised under both hydraulically rough and smooth conditions. Section 5 will then detail simulated boundary layer flows driven by measured tsunami signals from the field, which will be reconciled with those of the synthetic cases considered previously. Conclusions will finally be drawn in Section 6.

## 2. Numerical Model

The numerical model utilised within the present work corresponds to the MatRANS model originally developed and described by Fuhrman et al. (2013), but now extended to incorporate a transitional turbulence closure model. Throughout the present work, the model is based on the horizontal component of the incompressible Reynolds-averaged Navier-Stokes (RANS) equations, which reads:

$$\frac{\partial u}{\partial t} = -\frac{1}{\rho} \frac{\partial p}{\partial x} + \nu \frac{\partial^2 u}{\partial y^2} + \frac{\partial}{\partial y} \left( \nu_T \frac{\partial u}{\partial y} \right), \quad (1)$$

where  $u$  is the horizontal velocity,  $x$  and  $y$  are, respectively, horizontal and vertical directions,  $t$  is time,  $p$  is the pressure,  $\rho$  the water density, and  $\nu$  the kinematic viscosity. In what follows unsteady wave boundary layer flows will be considered in the absence of a mean current, with the driving pressure gradient expressed as:

$$\frac{1}{\rho} \frac{\partial p}{\partial x} = -\frac{\partial u_0}{\partial t}, \quad (2)$$

where  $u_0$  is the desired free stream velocity signal, to be clarified in what follows.

The system is closed using a transitional variant of the standard two-equation  $k-\omega$  turbulence model of Wilcox (2006). The model consists of transport equations for the turbulent kinetic energy (per unit mass)  $k$ :

$$k = \frac{1}{2} \left( \overline{u'^2} + \overline{v'^2} + \overline{w'^2} \right), \quad (3)$$

as well as for the specific dissipation rate  $\omega$ , which are given by:

$$\frac{\partial k}{\partial t} = \nu_T \left( \frac{\partial u}{\partial y} \frac{\partial u}{\partial y} \right) - \beta^* k \omega + \frac{\partial}{\partial y} \left[ \left( \nu + \sigma^* \alpha^* \frac{k}{\omega} \right) \frac{\partial k}{\partial y} \right], \quad (4)$$

$$\begin{aligned} \frac{\partial \omega}{\partial t} &= \alpha \frac{\omega}{k} \nu_T \left( \frac{\partial u}{\partial y} \frac{\partial u}{\partial y} \right) - \beta \omega^2 \\ &\quad + \frac{\partial}{\partial y} \left[ \left( \nu + \sigma \alpha^* \frac{k}{\omega} \right) \frac{\partial \omega}{\partial y} \right] + \frac{\sigma_d}{\omega} \frac{\partial k}{\partial y} \frac{\partial \omega}{\partial y}. \end{aligned} \quad (5)$$

In (3) the prime superscripts indicate fluctuating turbulent velocity components, whereas the overbar denotes time (ensemble) averaging. The eddy (turbulence) viscosity  $\nu_T$  is defined according to:

$$\nu_T = \alpha^* \frac{k}{\omega}. \quad (6)$$

The following closure coefficients are kept constant:  $\beta_0 = 0.0708$ ,  $\beta_0^* = 9/100$ ,  $\sigma = 1/2$ ,  $\sigma^* = 3/5$ ,  $\sigma_{do} = 1/8$ ,  $\alpha_0^* = 1/3\beta_0$ ,  $\alpha_0 = 1/9$ , with:

$$\sigma_d = \mathcal{H} \left\{ \frac{\partial k}{\partial y} \frac{\partial \omega}{\partial y} \right\} \sigma_{do}, \quad (7)$$

where  $\mathcal{H}\{\cdot\}$  is the Heaviside step function taking a value of unity when the argument is positive and value of zero otherwise. Rather than being constants, as in more traditional high Reynolds number two-equation turbulence closures, the remaining closure coefficients depend on a so-called turbulence Reynolds number:

$$Re_T = \frac{k}{\omega \nu}, \quad (8)$$

which allows the model to capture the transition from laminar to turbulent conditions. The transitional coefficients are given by:

$$\alpha^* = \frac{\alpha_0^* + Re_T/R_k}{1 + Re_T/R_k}, \quad (9)$$

$$\alpha = \frac{13}{25} \frac{\alpha_0 + Re_T/R_\omega}{1 + Re_T/R_\omega} (\alpha^*)^{-1}, \quad (10)$$

$$\beta^* = \beta_0^* \frac{100 \beta_0/27 + (Re_T/R_\beta)^4}{1 + (Re_T/R_\beta)^4}, \quad (11)$$

where  $R_k = 3$ ,  $R_\omega = 2.61$ ,  $R_\beta = 8$ .

With regards to the boundary conditions, the top boundary acts as a frictionless rigid lid, with the vertical derivatives of  $k$ ,  $\omega$ , and  $u$  equal to zero. A no-slip  $u=0$  condition is implemented at the bottom. Similarly, a  $k=0$  bottom boundary condition is enforced. In conjunction with this boundary condition, note that the stress-limiting feature on the full eddy viscosity of Wilcox (2006) is switched off, to avoid potential polluting effects under hydraulically rough conditions, a problem identified and described in more detail by Fuhrman et al. (2010). The  $\omega$  bottom boundary condition is specified according to (Wilcox, 2006, p. 208):

$$\omega = \frac{U_f^2}{\nu} S_R, \quad y = 0 \quad (12)$$

$$S_R = \begin{cases} \left(\frac{200}{k_s^+}\right)^2, & k_s^+ \leq 5 \\ \frac{60}{k_s^+} + \left[\left(\frac{200}{k_s^+}\right)^2 - \frac{60}{k_s^+}\right] e^{5-k_s^+}, & k_s^+ > 5. \end{cases} \quad (13)$$

where  $k_s^+ = k_s U_f / \nu$  is the roughness Reynolds number, expressed in terms of Nikuradse's equivalent sand grain roughness  $k_s$  and the friction velocity  $U_f$ . Notice that it is only through the  $\omega$  bottom boundary condition that the effects of bottom roughness are incorporated.

As found previously with other transitional turbulence closure models (e.g. Blondeaux and Vittori, 2012), experience has shown that an initial  $k = 0$  condition across the model domain prohibits transition to turbulent conditions. As such, small initial disturbances in  $k$  and  $\omega$  are introduced uniformly across the model domain, corresponding to:  $k = 6 \times 10^{-4} U_{1m}^2$  and  $\omega = 10^{-8} U_{1m}^2 / \nu$ , where  $U_{1m}$  is the maximum amplitude of the free stream velocity, to be specified for each individual case in what follows.

The computational grids utilised in what follows consist of 100 logarithmically-stretched vertical points. As a  $k = 0$  boundary condition is utilised, the viscous sublayer is resolved in all simulations by ensuring that  $\Delta y^+ = \Delta y U_f / \nu \leq 1$ , where  $\Delta y$  is the size of the first grid above the bed. The above equations are solved in the Matlab environment, making use of standard finite difference approximations coupled with the built-in ODE time stepping schemes, again as described in Fuhrman et al. (2013).

### 3. Model Validation

#### 3.1. Single wave boundary layers

We will first validate the numerical model against experimental measurements of Sumer et al. (2010) who, using an oscillating tunnel, considered boundary layers generated by transient waves having free stream velocity signals of the form:

$$u_0 = U_{1m} \operatorname{sech}^2(\Omega t), \quad (14)$$

where  $\Omega = 2\pi/T$  is the angular frequency.  $T$  is interpreted as a characteristic period of motion corresponding to the time duration where the free stream flow exceeds  $0.05U_{1m}$ . The phase evolution of the free stream velocity (14) is shown in Figure 1. The corresponding Reynolds number will be denoted by:

$$Re = \frac{aU_{1m}}{\nu}, \quad (15)$$

where  $a = U_{1m}/\Omega$  is a characteristic length scale. While the velocity signal (14) is similar to that of solitary waves, the period  $T$  and velocity magnitude  $U_{1m}$  are independent of one another. To distinguish this characteristic, signals of the form (14) will be generally termed “single waves” in what follows.

The experiments of Sumer et al. (2010) provided shear stress and velocity measurements for a series of tests on hydraulically smooth beds over the range  $2.8 \times 10^4 \leq Re \leq 2 \times 10^6$ . The tests, all of which have been simulated numerically, are summarised in Table 1. Hydraulically smooth conditions are ensured in the model by fixing  $k_s$  such that  $k_s^+ < 1$  is maintained throughout the wave cycle. The oscillatory tunnel had a half tunnel height of  $h_m = 0.145$  m.

Figure 2 presents the phase evolution of the computed and measured horizontal velocity profiles for selected values of  $Re$ , ranging from laminar ( $Re = 7.1 \times 10^4$ , Figure 2a) to turbulent ( $Re = 1.8 \times 10^6$ , Figure 2c) conditions, across selected phases. The agreement between the computed and measured values is satisfactory across the flow depth for each  $Re$  considered. As shown in Figure 2a, the model accurately details the laminar flow reversal experienced in the near bed region during the deceleration stage. This is forced by the adverse pressure gradient coupled with additional shear stresses in the boundary layer. As  $Re$  is increased, the model adequately captures the decrease in the phase lead of the near-bed flow, e.g. in Figure 2c, as turbulence begins to form, initially in the deceleration stage, enhancing the vertical mixing of momentum.

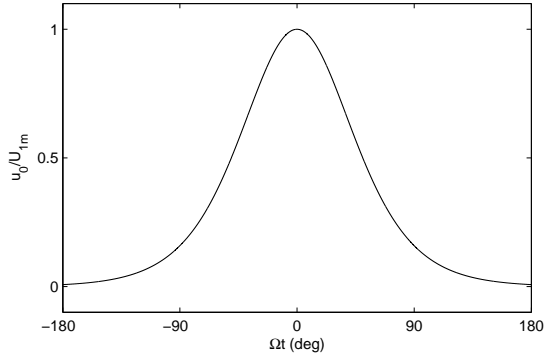


Figure 1: Phase evolution of the free stream velocity for a single wave.

As further validation, comparison of the computed and measured phase evolution of bed shear stress  $\tau_0$ , normalised by  $U_{1m}^2$ , for increasing  $Re$ , is presented in Figure 3. For  $Re < 2 \times 10^5$  (e.g. Figure 3a) the computed and measured bed shear stresses are in good agreement throughout the wave cycle, both closely following the analytical laminar solution of Liu et al. (2007). For  $Re > 2 \times 10^5$  the experimental bed shear begins to deviate from

Table 1: Summary of the single waves from Sumer et al. (2010) used in the model validation, with  $\nu = 1.0 \times 10^{-6} \text{ m}^2/\text{s}$ .

Test no.	$T(s)$	$U_{1m}$ (m/s)	$Re = aU_{1m}/\nu$
1	7.0	0.14	$2.8 \times 10^4$
2	8.4	0.21	$5.9 \times 10^4$
3	8.2	0.22	$7.1 \times 10^4$
4	8.8	0.25	$9.4 \times 10^4$
5	9.2	0.36	$2.0 \times 10^5$
6	9.3	0.41	$2.7 \times 10^5$
7	8.9	0.45	$3.1 \times 10^5$
8	9.4	0.53	$4.4 \times 10^5$
9	9.0	0.56	$4.8 \times 10^5$
10	9.3	0.64	$6.5 \times 10^5$
11	8.8	0.82	$1.1 \times 10^6$
12	8.3	0.96	$1.3 \times 10^6$
13	8.7	1.03	$1.6 \times 10^6$
14	7.8	1.20	$1.8 \times 10^6$
15	7.9	1.19	$2.0 \times 10^6$

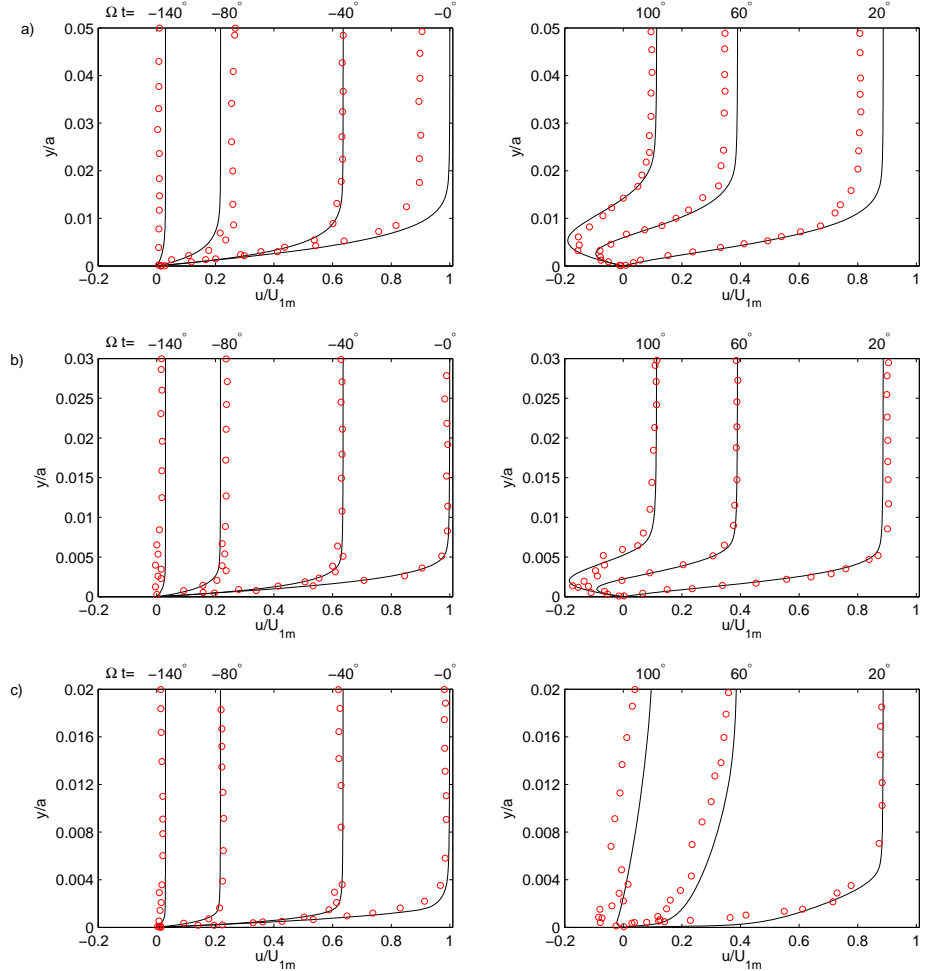


Figure 2: Comparison of computed (lines) and measured (circles, from Sumer et al., 2010) velocity profiles for single wave conditions on smooth beds corresponding to: (a) laminar conditions with  $Re = 7.1 \times 10^4$ , (b) transitional conditions with  $Re = 4.8 \times 10^5$ , and (c) turbulent conditions with  $Re = 1.8 \times 10^6$ . The left- and right-hand sub-plots correspond, respectively, to times of accelerating and decelerating free stream flow, see Figure 1.

the laminar solution in the deceleration phase. As described in Sumer et al. (2010), between  $2 \times 10^5 < Re < 5 \times 10^5$  (e.g. Figure 3b,c) this is due to the generation of two-dimensional vortex tubes. Such behaviour cannot be captured by the present, 1DV, model which continues to predict laminar behaviour across this range of  $Re$ . The experimental findings indicate that for  $Re > 5 \times 10^5$  (Figure 3d–f) the vortex tubes disintegrate to form turbulent spots. This is characterised by a sharp secondary turbulent peak in the bed shear stress signals, behaviour which is replicated by the model (e.g. Figure 3e,f). The model predicts the generation of appreciable levels of turbulence for  $Re > 7 \times 10^5$  prompting the transition towards turbulent conditions. Consistent with the experimental findings, turbulence initially forms after the near-bed flow reversal in the deceleration phase (e.g. Figure 3e), gradually transitioning to earlier phases as  $Re$  increases (e.g. Figure 3f). For sufficiently large  $Re$  the model correctly predicts that the secondary peak in the bed shear stress dominates the original laminar peak in the acceleration stage. The over-estimated peak in Figure 3f is likely, at least in part, to the ensemble averaging of the experimental results which will smooth out the reported peak experimental value relative to any single measurement. We note that the evolution of the modelled turbulence and bed shear stress signals is similar to that of Blondeaux and Vittori (2012) who, using a similar turbulence closure, also simulated the cases of Sumer et al. (2010).

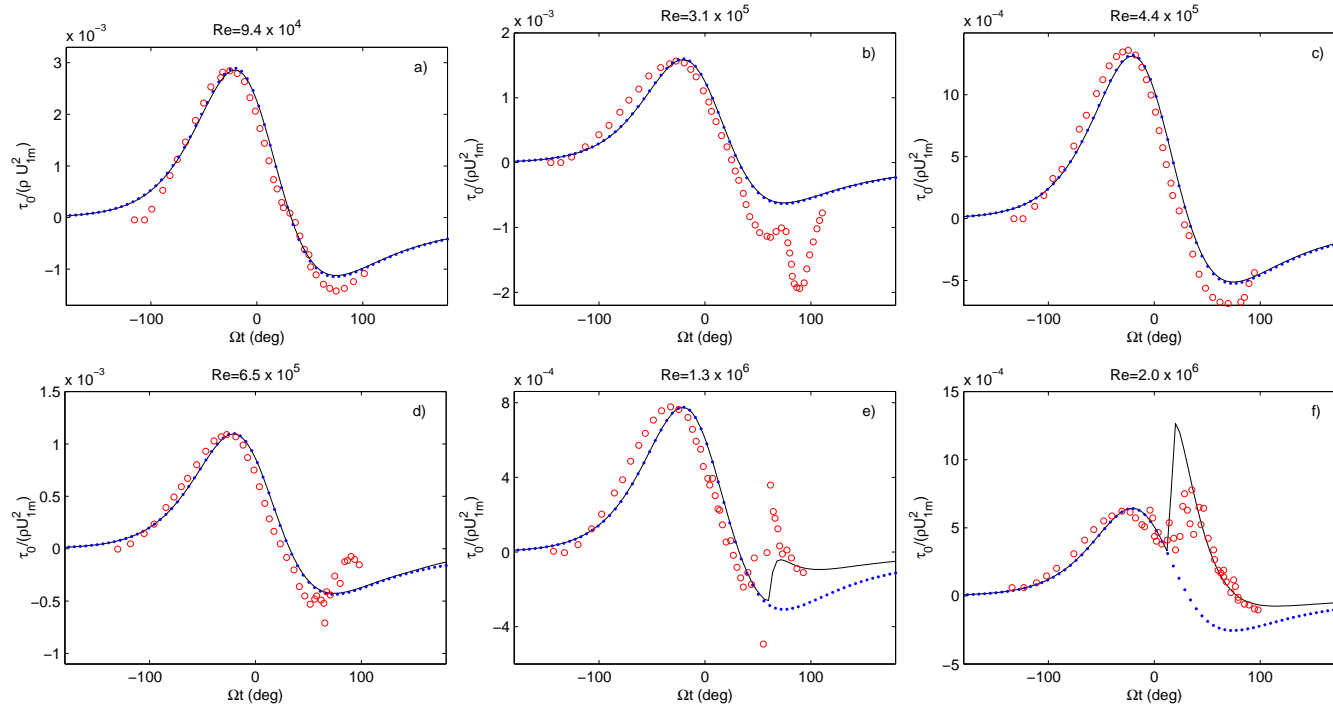


Figure 3: Comparison of computed (solid line) and measured (open circles, from Sumer et al., 2010) bed shear stress time series, for single waves on smooth beds with increasing Reynolds number. The dots depict the laminar solution of Liu et al. (2007).

The simulated bed shear stress signals will now be summarised by their maximum values  $\tau_{0,max}$  experienced during a wave cycle, in the form of wave friction factors,  $f_w$ , defined according to:

$$f_w = \frac{2\tau_{0,max}}{\rho U_{1m}^2}. \quad (16)$$

This parameter is monitored (when relevant) based on initial (laminar) peaks in the bed shear stress during acceleration phases, and for secondary (turbulent) peaks following transition. Based on dimensional grounds it is well known that  $f_w$  depends on  $Re$  under hydraulically smooth conditions. This is further demonstrated in Figure 4 which depicts a comparison between measured and computed values of  $f_w$ . The model accurately captures the measured peak in bed shear stress in the acceleration stage with both sets of values largely collapsing onto the laminar analytical solution of Liu et al. (2007). This indicates that, over the range of  $Re$  considered, the effects of turbulence are largely absent in the acceleration stages. Figure 4 also illustrates the rapid growth of the secondary turbulent peaks following their initial formation across larger  $Re$  values.

The preceding validation confirms the ability of the present model to

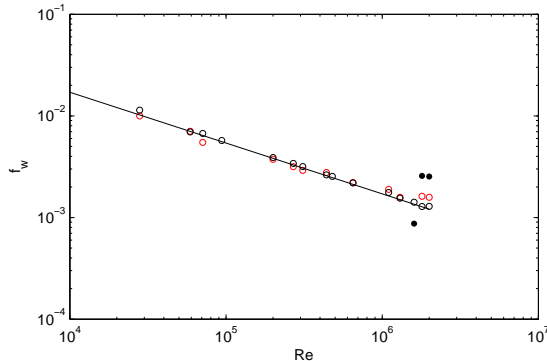


Figure 4: Comparsion between measured (red, from Sumer et al., 2010) and computed (black) wave friction factors for solitary waves under hydraulically smooth conditions. Open circles denote factors relating to peaks in bed shear stress during acceleration phases, whereas closed circles denote factors relating to the secondary (turbulent) peaks in the bed shear stresses during deceleration phases. The full line indicates the laminar solution of Liu et al. (2007).

correctly simulate the laminar flow regime for sufficiently small Reynolds numbers, as well as to predict reasonably the phase at which transition to turbulence occurs for transitional Reynolds numbers. Such behaviour cannot be simulated by more standard (i.e. non-transitional, “high Reynolds number”) turbulence closure models.

### 3.2. Rough-turbulent wave boundary layer

Finally, the model will be validated for unsteady flows on rough beds, as is often encountered in practice. A single experimental case (Case 13) from Jensen et al. (1989) will be considered, who studied boundary layers beneath oscillatory free stream velocity signals of the form:

$$u_0 = U_{1m} \sin(\Omega t) \quad (17)$$

within the same oscillatory tunnel as considered previously. With  $T = 9.72$  s,  $U_{1m} = 2.00$  m/s, and bottom roughness  $k_s = 0.84$  mm, the signal is typical of e.g. wind waves during storm conditions. Taking  $\nu = 1.12 \times 10^{-6}$  m<sup>2</sup>/s, these conditions yield  $Re = 6 \times 10^6$  and  $k_s^+ = 84$  i.e. hydraulically rough conditions. The capability of  $k - \omega$  models to simulate boundary layer flow induced by oscillatory waves is well known (e.g. Blondeaux, 1987; Blondeaux et al., 2012) consequently the present results, which are consistent with these studies, shall be only briefly discussed.

Figure 5 presents a comparison between the modelled and measured horizontal flow velocity profiles across the positive half cycle. The agreement between the measured and computed values is satisfactory across all phases with the model adequately details the lead of the near bed flow over the free stream velocity. The phase lead (roughly 15°) is less than that under laminar conditions for reasons analogous to those outlined previously for the solitary wave case.

Next, a comparison of the measured and computed turbulent kinetic energy density profiles over a half cycle is shown in Figure 6. The measured profiles are calculated from the two available measured fluctuating components according to  $k = 0.65 (\overline{u'^2} + \overline{v'^2})$  (Justesen, 1991). While not perfect, the computed profiles are generally consistent with the experimental data and are particularly accurate during the acceleration stage.

Finally, a comparison between the measured and computed phase evolution of the bed shear stress, presented here as the friction velocity,  $U_f = (\tau_0/\rho)^{0.5}$  normalised by  $U_{1m}$ , is depicted in Figure 7. The agreement between the modelled and computed values during the first half cycle is good,

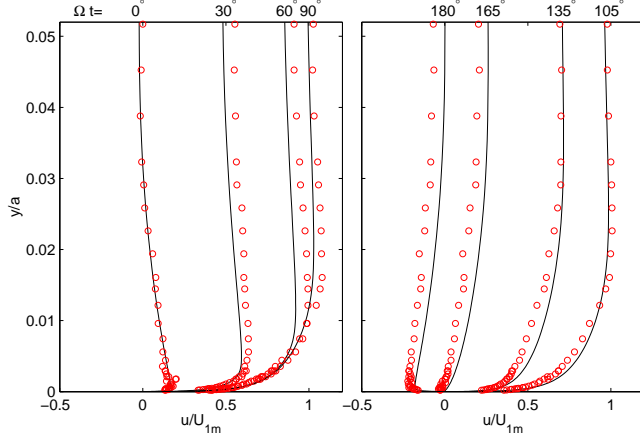


Figure 5: Comparison of computed (lines) and measured (circles, from Jensen et al., 1989) velocity profiles in an oscillatory boundary layer with  $Re = 6 \times 10^6$  and  $k_s^+ = 84$ .

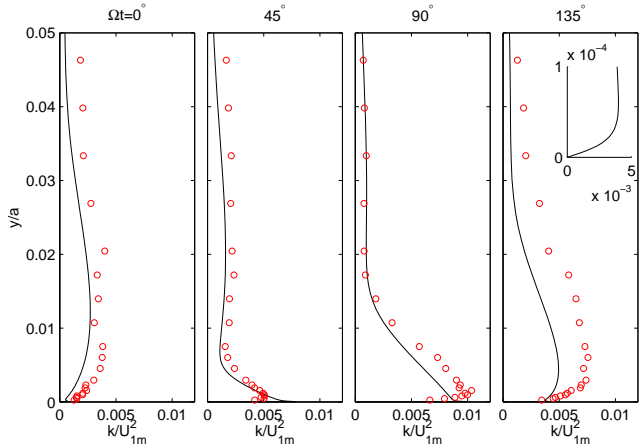


Figure 6: Comparison of computed (lines) and measured (circles, from Jensen et al., 1989) turbulent kinetic energy density  $k$  profiles in an oscillatory boundary layer with  $Re = 6 \times 10^6$  and  $k_s^+ = 84$ . The inset in the right most panel highlights the  $k = 0$  wall boundary condition.

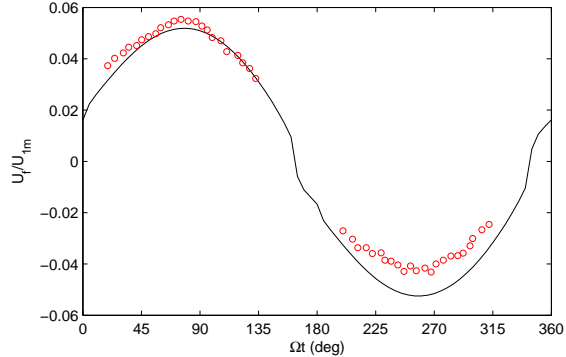


Figure 7: Comparison of computed (line) and measured (circles, from Jensen et al., 1989) friction velocity time series for an oscillatory boundary layer with  $Re = 6 \times 10^6$  and  $k_s^+ = 84$ .

with the model capturing the value and phase at which  $U_f$  attains its maximum value well. Given that the model predicts the same magnitude of the friction velocity in the positive and negative half cycles, as is expected for oscillatory flow, the discrepancy between measured and computed values in the negative half cycle are likely due to asymmetries in the experimental flow.

The preceding model validation, utilising experiments selected from Sumer et al. (2010) and Jensen et al. (1989), collectively demonstrates that the present model can accurately reproduce velocity profiles, turbulence quantities, and bed shear stresses in wave boundary layer flows, beneath both transient and oscillatory flows, on both smooth and rough beds. The smooth-bed single wave validation cases considered additionally demonstrate the ability of the model to reasonably capture laminar-to-turbulence transition, in contrast to many two-equation turbulence closures in the literature.

#### 4. Simulation of tsunami-scale wave boundary layers: Synthetic signals

Having successfully validated the model for velocity profiles, turbulence quantities, and bed shear stresses in the preceding section, it will now be utilised to simulate and study unsteady transient wave boundary layer processes at full tsunami scales. Due to their very large periods and long wavelengths, such scales can be difficult (if not impossible) to obtain within conventional laboratory settings, though they can be more readily reached

within numerical flow environments, as will be shown.

We will begin our numerical study of tsunami-scale wave boundary layers through systematic consideration of several idealised cases, deemed “synthetic” wave signals in what follows. For this purpose, signals having characteristic period  $T = 15$  min will be considered. This figure is well-known to be within a range typical of tsunamis, and also reasonably resembles observations from the 2004 Indian Ocean tsunami event (e.g. Madsen and Fuhrman, 2008). For the purposes of the present analysis, waves with this period will be given a reference offshore wave height  $H_0 = 1$  m corresponding to a water depth  $h_0 = 4000$  m, representing a typical average depth of Earth’s oceans. To generate a series of conditions spanning a realistic parametric range, this reference offshore condition will then be shoaled (based on energy flux conservation from linear shallow-water wave theory, for simplicity) to a number of additional depths according to:

$$\frac{H}{H_0} = \left( \frac{h_0}{h} \right)^{1/4}, \quad (18)$$

where  $H$  is the wave height at water depth  $h$ . For each depth considered the corresponding velocity magnitude  $U_{1m}$  is then calculated (again, based on linear shallow water theory) according to:

$$U_{1m} = \sqrt{\frac{gH^2}{4h}}. \quad (19)$$

A summary of the water depths and corresponding  $U_{1m}$  values to be considered are presented in Table 2. As seen there, 13 water depths ranging from  $h_0 = 4000$  m to  $h = 10$  m will be considered. In this manner,  $Re$  varies between  $8.7 \times 10^4$  and  $7.0 \times 10^8$ , i.e. conditions ranging from laminar to Reynolds numbers well beyond (by roughly two orders of magnitude) those typical of wind waves.

Table 2: Summary of input values used in the synthetic tsunami model simulations. The  $k_s^+$  values are determined from the computed single wave model runs.

$h$ (m)	$H$ (m)	$U_{1m}$ (m/s)	$a = \frac{U_{1m}}{\Omega}$ (m)	$Re = \frac{aU_{1m}}{\nu}$	$d = 0.3$ mm		$d = 1.5$ mm		$d = 3$ mm	
					$a/k_s$	$k_s^+ = \frac{k_s U_{fm}}{\nu}$	$a/k_s$	$k_s^+$	$a/k_s$	$k_s^+$
4000	1.00	0.0248	3.54	$8.7 \times 10^4$	4700	0.998	946	4.99	470	9.98
2000	1.19	0.0416	5.97	$2.5 \times 10^5$	7950	1.30	1590	6.47	795	13.0
1000	1.41	0.0700	10.0	$7.0 \times 10^5$	$1.34 \times 10^4$	1.67	2680	8.37	1340	16.7
900	1.45	0.0748	10.9	$8.2 \times 10^5$	$1.45 \times 10^4$	1.73	2900	8.65	1450	17.3
800	1.50	0.0828	11.9	$9.9 \times 10^5$	$1.58 \times 10^4$	1.82	3160	9.11	1580	18.2
700	1.55	0.0915	13.1	$1.2 \times 10^6$	$1.75 \times 10^4$	1.91	3500	9.59	1750	19.2
600	1.61	0.1027	14.7	$1.4 \times 10^6$	$1.96 \times 10^4$	2.03	3920	12.0	1960	28.4
500	1.68	0.118	16.9	$2.0 \times 10^6$	$2.25 \times 10^4$	3.89	4500	23.7	2250	51.2
200	2.11	0.234	33.5	$7.9 \times 10^6$	$4.47 \times 10^4$	6.79	8950	39.5	4470	83.5
100	2.51	0.394	56.4	$2.2 \times 10^7$	$7.52 \times 10^4$	11.5	$1.50 \times 10^4$	62.9	7521	135
50	2.99	0.662	94.9	$6.3 \times 10^8$	$1.26 \times 10^5$	18.2	$2.53 \times 10^4$	101	$1.27 \times 10^4$	219
20	3.76	1.32	189	$2.5 \times 10^8$	$2.51 \times 10^5$	33.8	$5.03 \times 10^4$	191	$2.52 \times 10^4$	422
10	4.50	2.21	317	$7.0 \times 10^8$	$4.23 \times 10^5$	53.6	$8.46 \times 10^4$	310	$4.23 \times 10^4$	684

Each of these wave conditions will be considered on a smooth bed, ensured by specifying sufficiently small roughness to keep  $k_s^+ \leq 1$  throughout the cycle, as before. Additionally, to examine the effects of bottom roughness three fixed grain sizes will also be considered:  $d = 0.3$  mm, 1.5 mm, and 3 mm, with the resulting equivalent bottom sand roughness calculated according to  $k_s = 2.5d$ . As shown in Table 2, the chosen parameters yield  $a/k_s$  varying from 470 to  $4.23 \times 10^5$ , again, extending well beyond values typical of wind-wave scales. Table 2 also presents typical  $k_s^+$  values encountered for each of three roughness values. As can be seen, the variation of roughness in this manner yields  $0.998 \leq k_s^+ \leq 684$  i.e. ranging from hydraulically smooth to well into the hydraulically rough regime (corresponding approximately to  $k_s^+ > 30$ ).

For each of the conditions described above, three separate synthetic wave signals will be considered. For simplicity, the first will correspond to a sinusoidal (oscillatory) wave, where the free stream velocity signal is given by (17). To achieve a periodic state when using this signal, the model is run for 10 full periods, with only the final period analyzed. The second signal will correspond to a single wave i.e. with the free stream velocity signal given by (14) and depicted in Figure 1; These cases will hence resemble those used previously in the model validation, but extending to much larger Reynolds numbers. As was noted in Section 3 single waves are similar in form to solitary waves, which represent a traditional paradigm in tsunami research (e.g. Synolakis, 1986, 1987; Yeh et al., 1994). We again stress, however, that (unlike solitary waves) in the present work the period  $T$  and wave height  $H$  (and hence the velocity magnitude  $U_{1m}$ ) are independent of

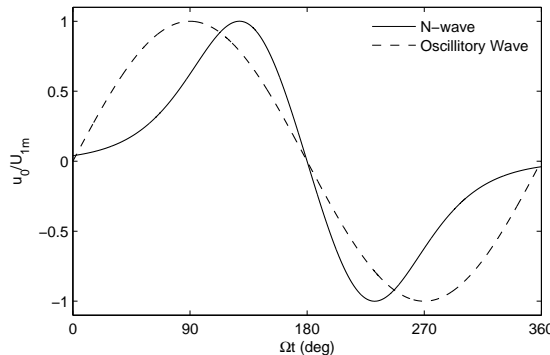


Figure 8: Phase evolution of the free stream velocity for N-wave (solid line) and oscillatory (dashed line) synthetic wave signals.

one another, as in reality. The third signal considered will correspond to so-called N-waves, a description proposed e.g. by Tadepalli and Synolakis (1994) and generalized for independent periods and wave heights in the run-up solution of Madsen and Schäffer (2010). Based on the free surface form described in Madsen and Schäffer (2010), the free stream velocity signal for these cases will be expressed as the superposition of two single waves:

$$u_0 = \Gamma U_{1m} \left\{ \operatorname{sech}^2 \left( \Omega t - \frac{3\pi}{4} \right) - \operatorname{sech}^2 \left( \Omega(t-t') - \frac{3\pi}{4} \right) \right\} \quad (20)$$

where  $t' = \pi/(2\Omega)$  is the relative phase shift of the second single wave and  $\Gamma = 1.165$  is a scaling factor added to ensure that  $u_{0,max} = U_{1m}$ . The corresponding N-wave free stream velocity signal is shown in Figure 8, together with the sinusoidal signal as a reference. Note that consideration of the waves as leading elevation or depression N-waves is dependent on how the positive flow direction is interpreted (similarly for the sinusoidal signal). As such, for the remainder of this work the positive and negative half-cycles shall be referred to as the leading and trailing cycles, respectively. Collectively, the 13 selected depths, combined with four bottom roughness values, and three wave signals, results in a (large, but manageable) computational matrix corresponding to  $13 \times 4 \times 3 = 156$  individual cases for simulation.

For each case the height of the model domain is set either to  $h_m = 0.4a$  or  $h_m = h$ , whichever is smaller. Preliminary testing has indicated that the value  $0.4a$  is more than sufficient to circumvent effects of depth limitation on the boundary layer, hence it is not necessary to resolve the entire physical depth to characterise the boundary layer processes. For cases where  $h_m = h$  was utilised (only relevant for the two depths with  $h \leq 20$  m) the model was also tested utilising identical forcing with the larger  $h_m = 0.4a$ . Consideration of bed shear stresses and turbulence profiles between the two runs (not shown for brevity) has indicated that even these positions are not affected by depth limitation. Hence, over the range of parameters considered, depth limitation effects are not significant, though they may be expected to play a more significant role e.g. if the depth were further reduced, corresponding to tsunami waves nearer to the shoreline. Note that such depth-limited effects on oscillatory boundary layers have been previously studied on rough beds by Tanaka et al. (1999).

To examine the flow structure at characteristic tsunami scales, Figure 9 presents the evolution of the horizontal velocity profiles at selected phases for each of the three wave signals considered. Results from hydraulically smooth (solid lines) and rough ( $d = 3$  mm, dashed lines) conditions are depicted, with  $Re = 2.2 \times 10^7$  and  $7.0 \times 10^8$  selected as typical examples. This figure is

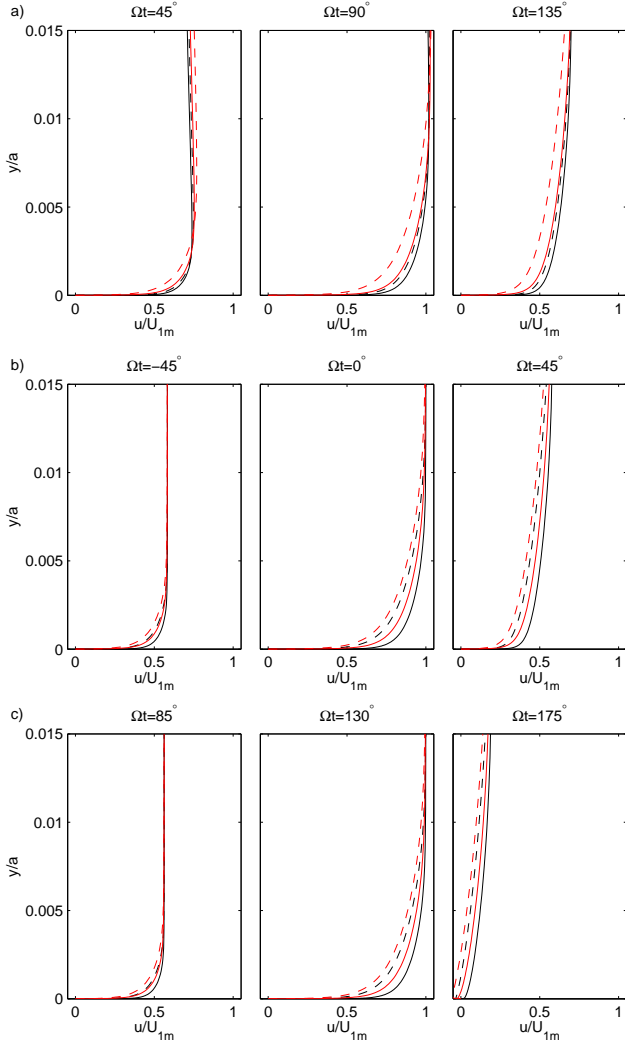


Figure 9: Computed velocity profiles under hydraulically smooth (solid lines) and rough (dashed lines, with fixed  $d = 3$  mm) conditions, beneath (a) oscillatory (sinusoidal), (b) single wave, and (c) N-wave signals. Results with  $Re = 7.0 \times 10^8$  (black) and  $Re = 2.2 \times 10^7$  (red) are depicted. See Table 2 for further details.

organised such that left-hand sub-plots corresponding to acceleration stages, middle sub-plots correspond to maximum free stream flow, and right-hand sub-plots correspond to deceleration stages. As seen, and consistent with

physical expectations, the presence of roughness acts to generally increase the boundary layer thickness and reduce near-bed flow velocities, with this effect diminishing with distance from the bed. The flow reduction is felt most strongly towards the end of the acceleration phase when the free stream flow is at or near its peak (see Figure 9, middle sub-plots).

Under hydraulically smooth conditions, the evolution of the flow velocities with increasing  $Re$  is similar, however the (non-dimensional) velocity gradients in the near wall region increase. The same is observed under hydraulically rough conditions with increasing  $a/k_s$ . In both cases, this is a consequence of a reduced (non-dimensional) boundary layer thickness. This is further demonstrated in Figure 10, which depicts the computed boundary layer thickness under both hydraulically smooth and rough conditions, for the sinusoidal wave cases. Note that for the hydraulically rough cases, only the results from those yielding  $k_s^+ > 30$  are depicted. Following Jensen et al. (1989), the boundary layer thickness  $\delta$  is here defined as the distance from the bottom to the maximum observed velocity at the peak free stream flow  $\Omega t = 90^\circ$ . As reference values, the boundary layer thicknesses based on existing expressions from Fredsøe and Deigaard (1992), typically applied at wind wave scales, will be shown. For example, for smooth beds they suggest the expression:

$$\frac{\delta}{a} = 0.086 Re^{-0.11}, \quad (21)$$

whereas for rough beds they suggest:

$$\frac{\delta}{a} = 0.09 \left( \frac{a}{k_s} \right)^{-0.18}. \quad (22)$$

These curves are depicted in Figure 10 as the dashed lines. For the larger values of  $Re$  and  $a/k_s$  considered here, which are again typical of full tsunami scales, the computed values of  $\delta/a$  tend to be somewhat (slightly) larger than predicted by these existing expressions, however. Improved fits based on results from the present simulations at full tsunami scales correspond to

$$\frac{\delta}{a} = 0.044 Re^{-0.07}, \quad (23)$$

$$\frac{\delta}{a} = 0.05 \left( \frac{a}{k_s} \right)^{-0.11}, \quad (24)$$

for the hydraulically smooth and rough conditions considered, respectively, which are depicted on Figure 10 as the full lines. Note also, that e.g. for the

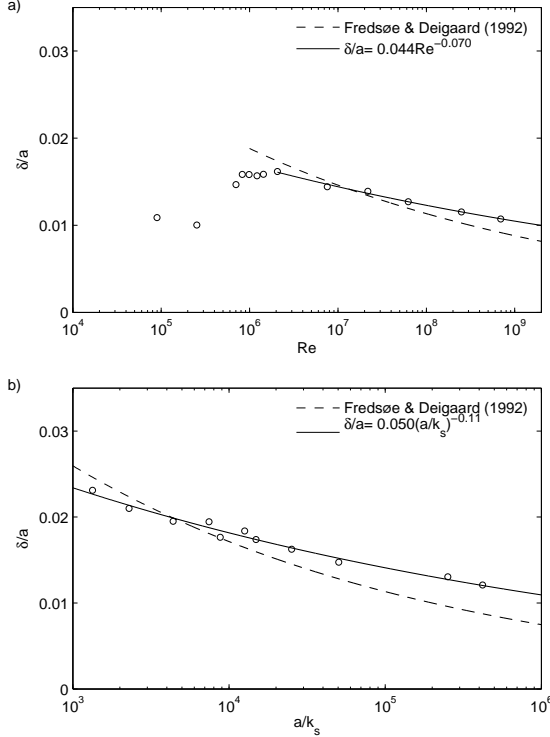


Figure 10: Non-dimensional boundary layer thickness for sinusoidal (oscillatory) waves under (a) hydraulically smooth conditions and (b) hydraulically rough conditions. Dashed lines denote expressions from Fredsøe and Deigaard (1992), whereas full lines correspond to either (23) or (24).

cases corresponding to the lowest depth considered i.e.  $h = 10$  m, the resulting wave boundary layer thickness is at most  $\delta \approx 0.015a \approx 5$  m. Hence, this further supports quantitatively our previous discussion that depth limitation effects are not significant over the parametric range being considered. This is consistent with a notion that the boundary layer beneath tsunami waves is fundamentally both current-like (due to their long durations), as well as wave-like, in the sense that the boundary layer is unsteady and may not extend over the entire water depth.

Understanding and quantifying the generation of turbulence within tsunami-scale boundary layers is similarly of interest, as turbulence is essential e.g. for putting and maintaining sediments in suspension, as well as in the diffusive transport of chemicals and other contaminants that may have settled on

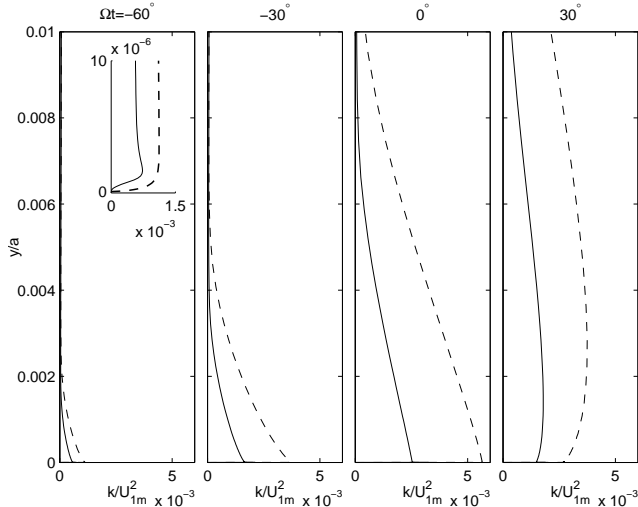


Figure 11: Computed turbulent kinetic energy density profiles for single wave cases with  $Re = 7.0 \times 10^8$  under hydraulically smooth (solid line) and rough (dashed line, grain size  $d = 3$  mm) conditions. The inset in the left most panel highlights the  $k = 0$  wall boundary condition.

the sea bed. As examples of the present results, Figure 11 illustrates the phase evolution of the turbulent kinetic energy density  $k$  profiles for the single wave cases with  $Re = 7.0 \times 10^8$ . Results are shown for both smooth and rough ( $d = 3$  mm) beds, for the sake of comparison. For large  $Re$  and  $a/k_s$  under both hydraulically smooth and rough conditions, appreciable turbulence is generated in the near bed region, even at early phases of the acceleration stage (i.e.  $\Omega t = -60^\circ$  in Figure 11), and continue to grow until the end of the acceleration stage (i.e.  $\Omega t = -30^\circ$  and  $0^\circ$ ). This behaviour is also mirrored in the N-wave and oscillatory signals (not shown separately for brevity). Unsurprisingly, the presence of roughness acts to enhance the production of the turbulence across the near bed region, with the effects becoming more pronounced towards the end of the acceleration stage. Into the deceleration stage ( $\Omega t = 30^\circ$  in Figure 11), there is a reduction in the production of turbulence near the bed, leaving the residual turbulence to be diffused upwards prior to being dissipated.

To quantify the turbulence generated for each of the synthetic wave forms considered, Figure 12 presents the maximum computed turbulence level,  $k_{max}$ , normalised by  $U_{1m}^2$ , observed during the various simulated wave cycles as a function of  $Re$  for the hydraulically smooth conditions ( $k_s^+ \leq 1$ )

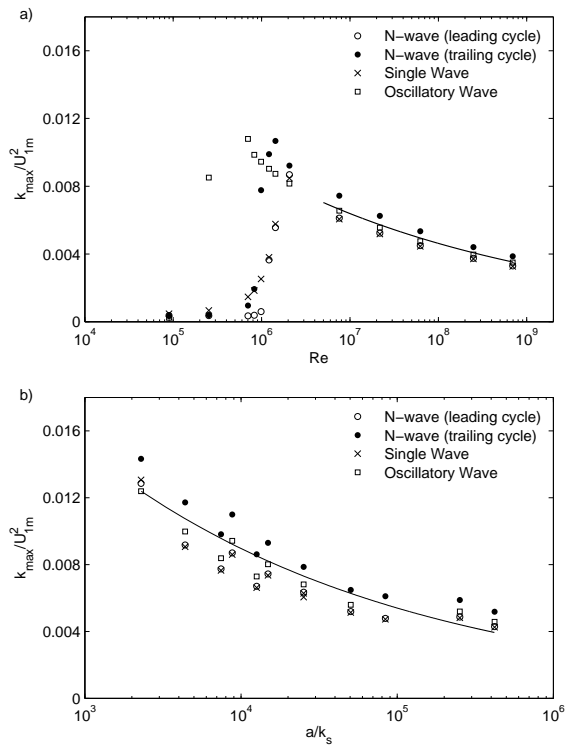


Figure 12: Maximum computed turbulent kinetic energy density observed during the synthetic tsunami wave cycles for: (a) hydraulically smooth conditions and (b) hydraulically rough conditions ( $k_s^+ > 30$ ). The solid lines in (a) and (b) respectively denote (25) and (26).

and a function of  $a/k_s$  for the hydraulically rough conditions (again, taken as  $k_s^+ > 30$ ) for each of the synthetic cases considered. Regarding the N-waves,  $k_{max}$  is monitored separately for both the leading and trailing cycles.

Under hydraulically smooth conditions, Figure 12a, the development of the normalised turbulence with increasing  $Re$  is generally similar for each of the wave signals. For small Reynolds numbers, such that the flow remains within the laminar regime, the turbulence expectedly is negligible. This is followed by a relatively rapid increase over a limited range of  $Re$ , marking the transition towards fully turbulent conditions. These trends are generally consistent with the behaviour seen previously during the model validation in Section 3, with results now extended to  $Re$  approaching  $10^9$ . Based on the present results, combined with e.g. Table 2, it is seen that tsunami-scale wave boundary layers can be expected to reach fully turbulent conditions out to water depths of say  $h = 500$  m or more i.e. in much deeper water than would be typical of wind wave scales. Consistent with experimental findings (Jensen et al., 1989; Sumer et al., 2010)  $k_{max}$  is initially observed to grow in the deceleration phase shortly after the flow reversal. The moment of transition then migrates to earlier phases with increasing  $Re$ . For the large Reynolds numbers typical of tsunamis in the nearshore, the transition to turbulence occurs so early that they can be well approximated as fully turbulent throughout their cycle, for most practical situations.

Interestingly, there are noticeable differences in the leading and trailing cycles of the N-wave signals. Across the  $Re$  considered, the trailing N-wave cycle consistently generates more turbulence than the leading cycle, which is seen to effectively collapse onto the single wave results. On the whole, the normalised turbulence values on Figure 12a for all of the wave types appear to converge reasonably as the  $Re$  approaches  $10^9$ . As a reference, the expression

$$\frac{k_{max}}{U_{1m}^2} = 0.061 Re^{-0.14} \quad (25)$$

is added as the full line, which represents the best collective fit in the fully turbulent regime. This expression can be used as a predictive base value for the maximum turbulent kinetic energy at full tsunami-scales on smooth beds, perhaps with slight adjustments made to the leading coefficient for the individual wave shapes considered herein.

The turbulence generated during hydraulically rough cases is similarly summarised on Figure 12b. Similar to experimental findings for oscillatory waves (Jensen et al., 1989; Sleath, 1987), under hydraulically rough conditions increasing values of  $a/k_s$  prompt a reduction in the normalised

turbulent kinetic energy density for each of the wave signals considered. Consistent with expectations based on the hydraulically smooth results just discussed, more turbulence is generated during the trailing cycle of the N-wave than in the leading cycle. This behaviour will be explained in more detail later within this section in connection to the induced bed shear stresses. As a reference, the curve

$$\frac{k_{max}}{U_{1m}^2} = 0.068 \left( \frac{a}{k_s} \right)^{-0.22} \quad (26)$$

is likewise added as the full line on Figure 12b, which represents best fit through entire  $a/k_s$  space studied for the various wave signals combined.

We will now turn our attention to quantification of the bed shear stresses found beneath the various synthetic wave types. As typical examples, Figure 13 shows the phase evolution of the bed shear stress  $\tau_0$ , normalised by its maximum value attained during the wave cycle  $|\tau_0|_{max}$ , under hydraulically smooth conditions. A separate sub-plot is shown for the three wave signals considered, each containing results for two selected high values of  $Re$ .

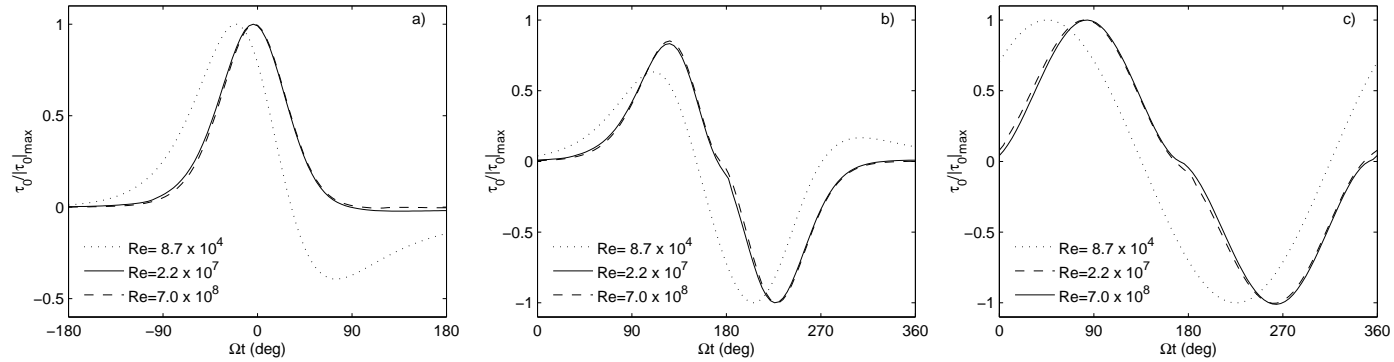


Figure 13: Phase evolution of the normalised bed shear stress on smooth beds at high Reynolds numbers for (a) single wave, (b) N-wave, and (c) sinusoidal (oscillatory) wave signals. The phase evolution of the normalised laminar bed shear stress (dots) is also shown for comparison.

Also shown as a reference, is the laminar solution (dotted lines). As seen, at typical tsunami scales, in contrast to the laboratory scales considered within Section 3, the bed shear stress effectively deviates from the laminar solution at all phases. This is consistent with observation that turbulence has spread into the acceleration phases, as discussed previously in connection with Figure 12. As with the velocity evolution shown in Figure 9, across each of the wave signals, the form of  $\tau_0$  does not change significantly as  $Re$  is increased. Again, at these scales fully turbulent conditions are reached very early in the cycle, such that transitional effects are marginalised, in contrast e.g. to the previously considered laboratory experiments of Sumer et al. (2010). The phases at which the peak shear stresses and near bed flow reversals occur become largely fixed, with the corresponding phase lead over the free stream velocity signal  $u_0$  much reduced compared to the laminar case. Results under hydraulically rough conditions are qualitatively similar to the fully-turbulent results presented in Figure 13.

The results for the bed shear stresses will now be summarised through consideration of the computed wave friction factors, again defined by (16). As before,  $f_w$  is considered separately for the leading and trailing N-wave cycles. Figure 14a presents the friction factors under hydraulically smooth conditions as a function of  $Re$ . For small values of  $Re$  (here representing tsunami conditions far offshore i.e. with large depth  $h$ , see again Table 2)  $f_w$  is associated with the laminar peaks in the bed shear stress occurring during the acceleration phases. In this regime, the corresponding  $f_w$  values for oscillatory and single waves collapse onto the expected analytical laminar solutions (e.g. Batchelor, 1967; Liu et al., 2007). Following transition to turbulence at larger Reynolds number i.e. roughly  $Re > 10^6$ , the computed friction factors associated with each of the wave types follow similar, well behaved, decreasing trends through to the largest  $Re$  numbers considered. The observed decreasing trends in the turbulent regime follow reasonably the empirical relation taken from Fuhrman et al. (2013):

$$f_w = 0.04Re^{-0.16}, \quad (27)$$

which closely resembles eq. (2.55) of Fredsøe and Deigaard (1992) i.e. their lead coefficient is changed slightly from 0.035 to 0.04 above. It is emphasised that the range of  $Re$  considered in the present study with focus on tsunami scales extends well beyond the range  $Re < 10^7$  originally used to formulate (27), thus suggesting that the development of peak bed shear stresses at full tsunami scales can be treated as part of a continuum with smaller wind-wave scale waves.

Regarding the considered N-wave signals, the computed friction factors corresponding to the leading half-cycle are seen to collapse onto the single wave values. This is unsurprising, given the general similarity in the driving pressure gradients across the acceleration stage for these two signals. From Figure 14 it is also seen that the peak bed shear stress associated with the trailing N-wave half cycle is consistently larger than the leading half-cycle. This is a consequence of the boundary layer having shorter time to develop during the trailing cycle as compared to the leading cycle (see again Figure 8) i.e. the time taken from flow reversal to the trough is comparatively short, hence resulting in reduced boundary layer thickness, larger velocity gradients, and larger shear stresses within the boundary layer. This also

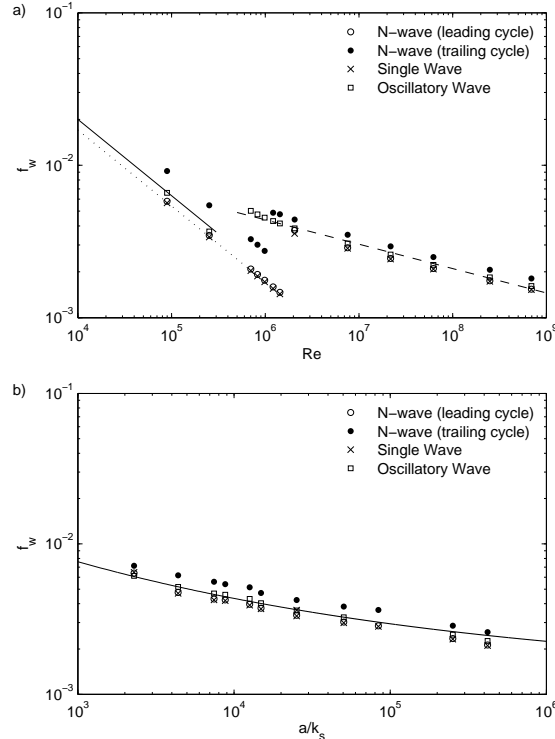


Figure 14: Computed wave friction factors for the various synthetic tsunami wave signals considered under (a) hydraulically smooth and (b) hydraulically rough conditions ( $k_s^+ > 30$ ). On (a) the dotted and full line respectively depict the laminar solutions for single waves and oscillatory signals, whereas the dashed line corresponds to (27). On (b) the full line depicts (28).

explains the asymmetric turbulence levels found for the leading and trailing N-wave half cycles, as discussed previously in connection with Figure 12. The difference in  $f_w$  between the leading and trailing N-wave cycles is generally less in the turbulent regime than in the laminar regime, however.

Figure 14b similarly presents the computed tsunami wave friction factors as a function of  $a/k_s$  for hydraulically rough conditions ( $k_s^+ > 30$ ). Across each of the wave signals  $f_w$  exhibits similar, relatively well behaved decreasing trends with increasing  $a/k_s$ . As with the hydraulically smooth conditions,  $f_w$  for the trailing N-wave cycle is consistently larger than the leading cycle whose values are again equivalent to the corresponding single wave. Relating this result to sediment transport, it would seemingly suggest the potential for tsunamis to result in enhanced transport rates during the trailing wave of tsunamis, at least for cases where the N-wave description adopted herein can be taken as representative. The behavior of  $f_w$  for the oscillatory waves largely collapses onto the corresponding empirically derived relation of Fuhrman et al. (2013):

$$f_w = \exp \left( 5.5 \left( \frac{a}{k_s} \right)^{-0.16} - 6.7 \right), \quad (28)$$

which was modified slightly from eq. (1.2.23) of Nielsen (1992). It is again emphasized that the range of  $a/k_s$  examined here extends well beyond the range (approximately  $a/k_s < 10^4$ ) over which (28) was originally formulated, again indicating a generally consistent evolution of bed shear stresses from wind-wave to much larger tsunami scales.

## 5. Tsunami-scale wave boundary layers: Measured signals

Having systematically investigated the boundary layers generated by various synthetic tsunami wave signals in the preceding section, we will finally investigate their relation to the boundary layers that develop beneath actual measured tsunami signals from the field. The motivation is to specifically examine the applicability of the various synthetic wave forms used in Section 4 for describing expected boundary layer properties beneath real geophysical tsunamis. For this purpose, two measured tsunami signals will be considered, one stemming from the 2011 Tohoku tsunami (measured by the GPS-based station Iwate South at a depth  $h_0 = 204$  m, see e.g. Chan and Liu, 2012), and one from the 2004 Indian Ocean tsunami (measured off the yacht Mercator at approximate depth  $h_0 = 14$  m, see e.g. Madsen and Fuhrman, 2008).

Table 3: Coefficients for the superposition of single waves used to approximate measured tsunami signals, and the corresponding water depth  $h_0$  at which the signal was measured. Note that the coefficients in parentheses have units of (m, s<sup>-1</sup>, s).

Tsunami	$h$ (m)	$(H_1, \Omega_1, t_1)$	$(H_2, \Omega_2, t_2)$	$(H_3, \Omega_3, t_3)$
Indian Ocean (2004)	14	(-3.10, 0.00420, 600)	(3.80, 0.00530, 1000)	(-1.00, 0.00900, 1399)
Tohoku (2011)	204	(-0.80, 0.00298, 580)	(2.20, 0.00330, 980)	(5.85, 0.0109, 1298)

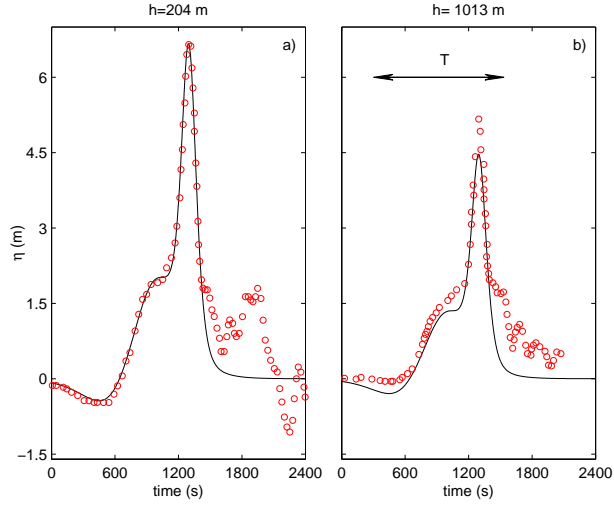


Figure 15: Comparison between estimated (line) and measured (circles) free surface elevations for the 2011 Tohoku tsunami at water depths (a)  $h_0 = 204$  m and (b)  $h = 1034$  m. The estimated free surface elevation in (b) is calculated via shoaling wave heights from (a).

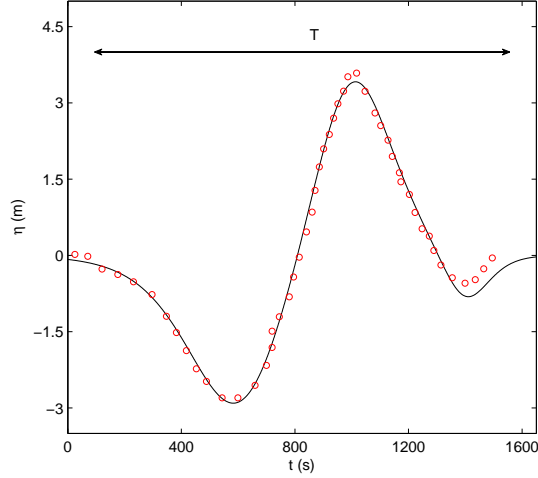


Figure 16: Comparison between estimated (line) and measured (circles) free surface elevations for the 2004 Indian Ocean tsunami measured at a water depth  $h_0 = 14$  m.

Chan and Liu (2012) found that the leading wave of the measured free surface elevation  $\eta(t)$  time series relating to the 2011 Tohoku tsunami could be well approximated by the superposition of three single waves of varying wave height and period described by:

$$\eta(t) = \sum_{n=1}^3 H_n \operatorname{sech}^2 \{\Omega_n (t - (t_0 + t_n))\}, \quad (29)$$

where  $t_0$  is a reference time and  $t_n$  represents a time shift. Similarly, Schimmele et al. (2014, 2016) found that the leading wave surface elevation corresponding to the 2004 Indian Ocean tsunami could also be reasonably well described through this methodology. The corresponding input coefficients for the description of these two signals are given in Table 3, where  $t_0 = 0$  in all cases. A comparison between the measured (circles) and fitted (line) signals for these two measured events is presented in Figure 15a and 16, respectively, which illustrates the close match achieved for the description of the leading tsunami waves. From these, it can also be readily observed that the form of the two tsunami signals are rather different. In relation to the three signals considered in Section 4, the Tohoku signal (Figure 15a) bares most resemblance to a single wave, whilst the Indian Ocean signal (Figure 16) is more reminiscent of an N-wave, though it could likewise also be reasonably characterised as approximately sinusoidal, as well.

For the present purposes, the surface elevations  $\eta(t)$  described by (29) will be converted into free stream velocity signals according to linear shallow water theory:

$$u_0 = \sqrt{\frac{g}{h}} \eta(t). \quad (30)$$

This is consistent with our previous approach, as well as with the findings of Chan and Liu (2012) i.e. that the leading tsunami waves in both near-field and far-field regions correspond to small amplitude long waves. The time derivative of (30) is then invoked directly within (2) for the driving pressure gradient. Additionally, the wave heights of the respective single wave components are shoaled from their measured water depths according to (18), thus allowing for the analytical signals to be applied at the other water depths considered in Section 4, as listed in Table 2. As a check of this procedure, Figure 15b presents a comparison of the derived free surface elevations calculated through the shoaling method and the corresponding measured values for the 2011 Tohoku tsunami, now taken from the ocean bottom pressure gage station TM2 at depth  $h = 1013$  m (see again Chan and Liu, 2012). The agreement is indeed seen to be satisfactory, hence indicating

that the present simple methodology can be utilised to reasonably capture the tsunami wave transformation to other water depths. Obviously, three-dimensional effects are in no way accounted for in this procedure.

In direct analogy to the single and N-waves considered previously, the period of each tsunami signal will be defined for the present purposes as the total time duration in which the free stream velocity signal exceeds 5% of its maximum value. The resulting effective periods for these two signals are shown in Figure 15b and 16, respectively. This in turn allows the Reynolds number to be defined through (15) where  $U_{1m} = u_{0,max}$ . For each water depth considered the roughness is again systematically varied, as outlined in Section 4 i.e. utilising hydraulically smooth conditions in addition to the same three roughness values as before. Collectively, the two wave signals, combined with 13 water depths and four bottom roughness values yield a computational matrix consisting of  $13 \times 4 \times 2 = 104$  different simulations, in addition to those previously considered.

Regarding the Indian Ocean signal, which again most closely resembles the synthetic N-wave description, friction factors and normalised turbulence measures will be considered separately for both the leading and trailing half-cycles. These cycles correspond to the first and second single wave used in the superposition of the free surface elevation signal (see Table 3). The computed  $k_{max}$  values (normalized by  $U_{1m}^2$ ), under both hydraulically smooth and rough conditions, are presented in Figure 17a and Figure 17b. Additionally, Figure 18a and 18b similarly presents a summary of computed tsunami wave friction factors. Also shown for comparison are the N-wave results taken from Figures 12 and 14, as well as the reference curves (25), (26), (27), and (28). For both hydraulic conditions the normalised turbulence and wave friction factors associated with the trailing cycle largely collapse onto the trailing N-wave trends determined in Section 4 across both the laminar and turbulent regimes. Consequently for this cycle, boundary layer aspects of the measured tsunami signal are indeed seen to be reasonably well approximated by the N-wave signal. However, the turbulence quantities and  $f_w$  associated with the leading cycle are consistently smaller than the corresponding leading N-waves cycle. This is unsurprising as the input single wave for this cycle has a relatively longer period and smaller magnitude free stream velocity than that of the trailing cycle. As such, these effects combine to reduce shear stresses and turbulence generation in the boundary layer for this half-cycle (see Figure 16). Nevertheless, the N-wave description captures the general behaviour well.

Similarly, Figure 19 and Figure 20 present summaries of the normalized turbulence and tsunami wave friction factors computed for the 2011 Tohoku

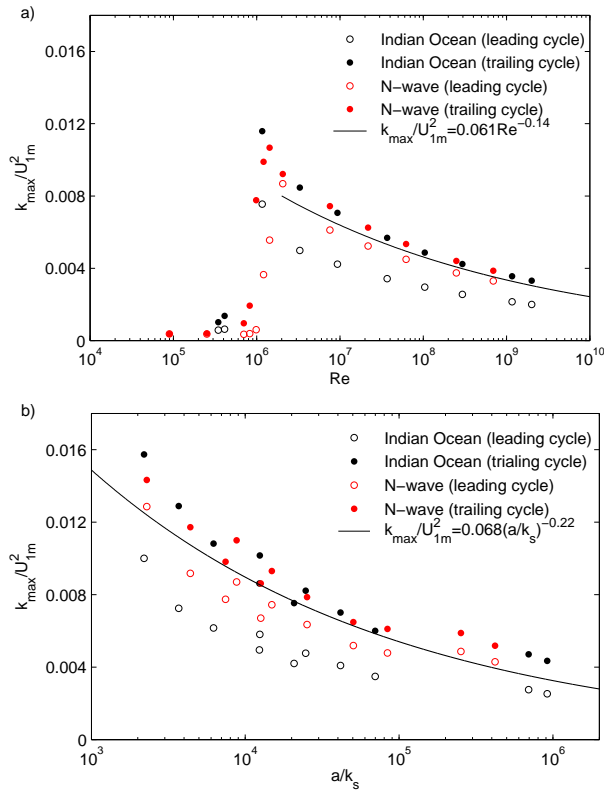


Figure 17: Maximum turbulent kinetic energy density observed during the simulated 2004 Indian Ocean tsunami under (a) hydraulically smooth and (b) hydraulically rough conditions. Also shown are the corresponding values for the leading and trailing N-wave cycles, for comparison.

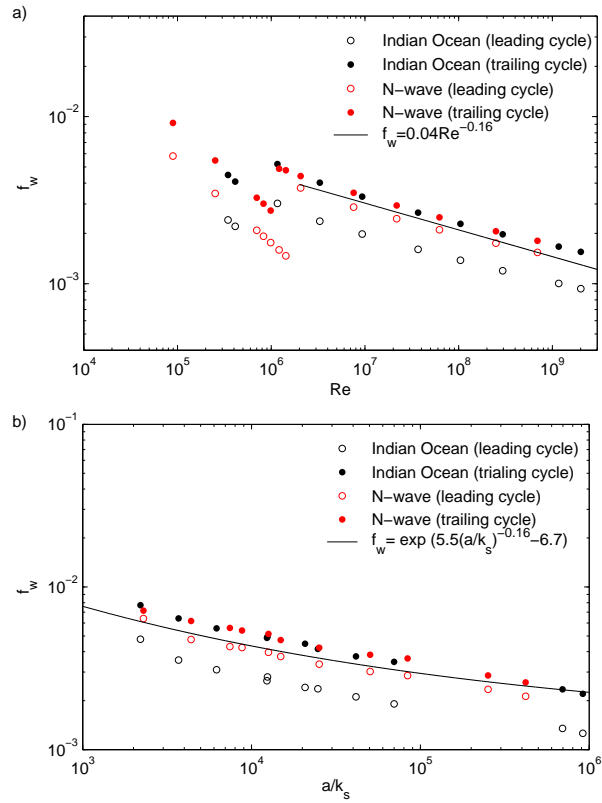


Figure 18: Computed wave friction factors relating to the 2004 Indian Ocean tsunami under (a) hydraulically smooth and (b) hydraulically rough conditions. Also shown are the corresponding values for the leading and trailing N-wave cycles, for comparison.

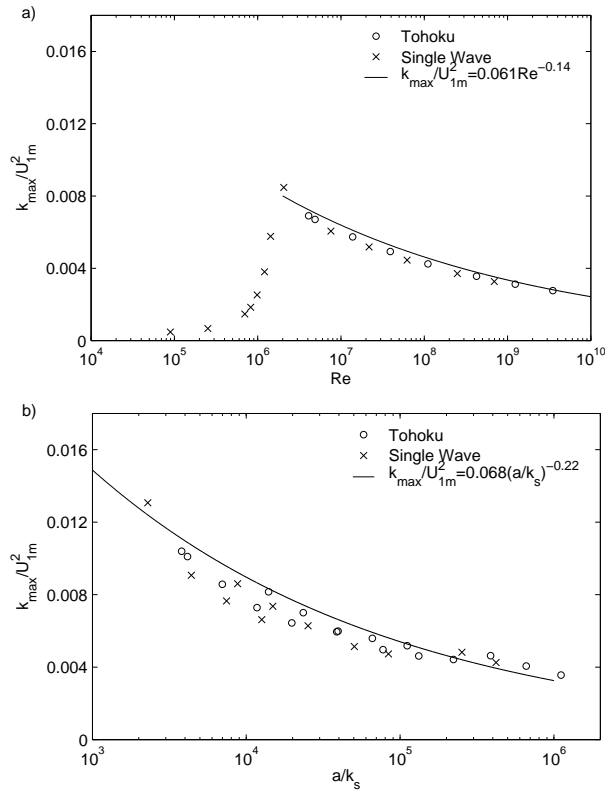


Figure 19: Maximum turbulent kinetic energy density observed during the simulated 2011 Tohoku tsunami under (a) hydraulically smooth and (b) hydraulically rough conditions. Also shown are the corresponding values for the synthetic single wave cases, for comparison.

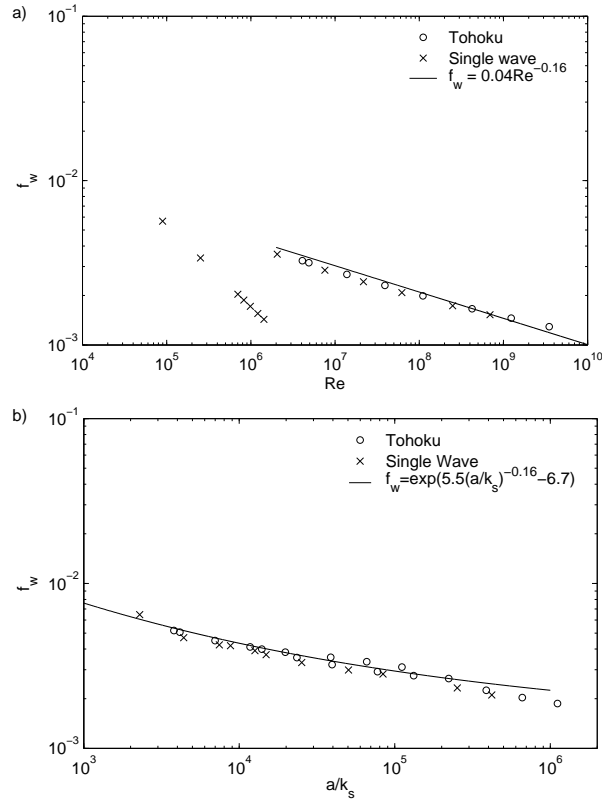


Figure 20: Computed wave friction factors relating to the 2011 Tohoku tsunami under (a) hydraulically smooth and (b) hydraulically rough conditions. Also shown are the corresponding values for the synthetic single wave cases, for comparison.

event, again under both hydraulically smooth and rough conditions. Also shown for comparison are now the single wave results taken from Figures 12 and 14, in addition to the previously mentioned reference curves (full lines). In contrast to the 2004 Indian Ocean tsunami, the computed normalised turbulence quantities and friction factors now effectively collapse to the corresponding single wave trends determined in Section 4 under both hydraulic conditions. This likewise confirms that a single wave description has the capacity to approximate the boundary layer flow and characteristics beneath realistic tsunami events.

The precise form of real geophysical tsunamis can vary greatly, and will inevitably depend on the precise nature of the generating seabed displacement. The reasonable match in the bed shear stresses and boundary layer turbulence generated beneath idealised and measured tsunami signals demonstrated in this section supports the use of both e.g. single waves and N-waves as representative design waves for inducing boundary layer flow and other characteristics typical of tsunamis, e.g. for potential use in future numerical or experimental research involving sediment transport or scour processes. Given the variety of tsunami shapes that can be expected in nature, and the reasonable similarity seen between all three synthetic wave forms, a sinusoidal description would also seemingly be a reasonable idealisation. In all cases, regardless of the specific wave form, the importance of maintaining independent period and wave height (and hence velocity magnitude) is emphasised.

## 6. Conclusions

An existing numerical one-dimensional vertical (1DV) model for simulating simple turbulent boundary layer flows (Fuhrman et al., 2013), based on the horizontal component of the incompressible Reynolds-Averaged Navier-Stokes (RANS) equations, has been newly extended to incorporate a transitional two-equation  $k-\omega$  turbulence closure. The developed model has been successfully validated against experimental measurements made in oscillating tunnel environments for both transient single wave (solitary-like, but with independent velocity magnitude and effective duration, as considered by Sumer et al., 2010) as well as oscillatory flows (Jensen et al., 1989). The comparisons against the experimental data sets collectively demonstrate the ability of the model to produce accurate flow velocities, bed shear stresses, and turbulent kinetic energy within the boundary layer, under both hydraulically smooth and rough conditions. Use of the transitional turbulence closure is also demonstrated to predict the intra-wave laminar-to-turbulence

transition that occurs at moderate Reynolds numbers with reasonable accuracy.

The validated model has subsequently been employed for the study of transient wave boundary layers at full characteristic tsunami scales. For this purpose, three different synthetic wave signals have been considered i.e. utilizing: (1) sinusoidal wave, (2) single wave, and (3) N-wave descriptions. A variety of realistic geophysical tsunami conditions have been generated, starting with characteristic offshore tsunami wave conditions (i.e. wave height  $H_0 = 1$  m at an offshore depth  $h_0 = 4000$  m), which are then shoaled to additional depths as shallow as  $h = 10$  m based on linear shallow water wave theory. The flow beneath each wave type and water depth combination considered is then simulated, considering four different values of the bottom roughness, selected to yield conditions ranging from hydraulically smooth to those with a fixed sediment grain diameter up to  $d = 3$  mm. This process yields a wide and realistic parametric range likely to be encountered beneath geophysical tsunami waves, in terms of the flow duration, associated Reynolds numbers (ranging from laminar conditions up to roughly  $10^9$ ), and dimensionless bottom roughness.

The resulting flow, wave boundary layer thickness, maximum turbulent kinetic energy, and maximum bed shear stresses have then been systematically parameterised and quantified, separately for hydraulically smooth and rough regimes. The simulations suggest that, over the range of conditions considered, the tsunami wave boundary layer thickness will grow to  $O(1$  m) and typically not be limited by the water depth at locations sufficiently offshore. This implies that the tsunami-generated boundary layer flows can be considered as both current-like due to their long duration, but also wave-like in the sense that their boundary layers are unsteady and will not necessarily span the entirety of the water column. New expressions for the boundary layer thickness and maximum turbulent kinetic energy density at the simulated tsunami scales are provided for both hydraulically smooth and rough beds. Additionally, the collective results for the maximum bed shear stresses (in the form of wave friction factor diagrams) suggest that existing expressions, originally developed for wind wave scales, can be extrapolated reasonably to full tsunami scales i.e. that there exists a continuum connecting these two scales.

As a final check of the validity of the various synthetic wave signals considered, the boundary layers developing beneath two real tsunami signals, stemming respectively from the 2004 Indian Ocean and 2011 Tohoku events, have additionally been considered. For the purposes of simulation, the leading waves from these measurements have been approximated based

on a superposition of single waves, as originally described by Chan and Liu (2012). While the form of these two measured signals differed substantially, it is shown that the boundary layers beneath the 2004 Indian Ocean and 2011 Tohoku events can, respectively, be quite reasonably characterised e.g. by the considered N-wave and single-wave descriptions considered previously. Given the wide variety of tsunami wave forms that can be expected in practice, depending on the nature of the generating bottom motions, it is likely that all three of the synthetic wave descriptions considered in the present work can be taken as realistic idealisations, appropriate for use in further numerical or experimental studies. Regardless of the wave form, the importance of maintaining independent periods and wave height (hence velocity magnitude) is emphasised.

## 7. Acknowledgement

The second author would like to acknowledge financial support from the European Union project ASTARTE: Assessment, Strategy And Risk Reduction for Tsunamis in Europe (FP7-ENV-2013.6.4-3, Grant number 603839). This support is greatly appreciated.

## 8. References

- Batchelor, G. K., 1967. An Introduction to fluid Mechanics. Cambridge University Press.
- Blondeaux, P., 1987. Turbulent boundary layer at the bottom of gravity waves. *J. Hydraul. Res.* 25, 447–463.
- Blondeaux, P., Vittori, G., 2012. RANS modelling of the turbulent boundary layer under a solitary wave. *Coast. Eng.* 60, 1–10.
- Blondeaux, P., Vittori, G., Bruschi, A., Lalli, F., Pesarino, V., 2012. Steady streaming and sediment transport at the bottom of sea waves. *J. Fluid Mech.* 697, 115–149.
- Chan, I.-C., Liu, P. L.-F., 2012. On the runup of long waves on a plane beach. *J. Geophys. Res.* 117, C08006.
- Fredsøe, J., Deigaard, R., 1992. Mechanics of Coastal Sediment Transport. World Scientific, Singapore.

- Fuhrman, D. R., Dixen, M., Jacobsen, N. G., 2010. Physically-consistent wall boundary conditions for the  $k-\omega$  turbulence model. *J. Hydraul. Res.* 48, 793–800.
- Fuhrman, D. R., Schløer, S., Sterner, J., 2013. RANS-based simulation of turbulent wave boundary layer and sheet-flow sediment transport processes. *Coast. Eng.* 73, 151–166.
- Jensen, B. L., Sumer, B. M., Fredsøe, J., 1989. Turbulent oscillatory boundary layers at high Reynolds numbers. *J. Fluid Mech.* 206, 265–297.
- Justesen, P., 1991. A note on turbulence calculations in the wave boundary layer. *J. Hydraul. Res.* 29, 699–711.
- Liu, P. L.-F., Park, Y. S., Cowen, E. A., 2007. Boundary layer flow and bed shear stress under a solitary wave. *J. Fluid Mech.* 574, 449 – 463.
- Madsen, P. A., Fuhrman, D. R., 2008. Run-up of tsunamis and long waves in terms of surf-similarity. *Coast. Eng.* 55, 209–223.
- Madsen, P. A., Fuhrman, D. R., Schäffer, H. A., 2008. On the solitary wave paradigm for tsunamis. *J. Geophys. Res.* 113, C12012/1–22.
- Madsen, P. A., Schäffer, H. A., 2010. Analytical solutions for tsunami runup on a plane beach: single waves, n-waves and transient waves. *J. Fluid Mech.* 645, 27–57.
- Menter, F. R., 1994. Two-equation eddy-viscosity turbulence models for engineering applications. *AIAA J.* 32 (8), 1598–1605.
- Nielsen, P., 1992. Coastal Bottom Boundary Layers and Sediment Transport. World Scientific, Singapore.
- Saffman, P. G., 1970. A model for inhomogeneous turbulent flow. *Proceedings of the Royal Society* 317 (1530), 417–433.
- Schimmels, S., Sriram, V., Didenkulova, I., 2016. Tsunami generation in a large scale experimental facility. *Coast. Eng.*, (in press).
- Schimmels, S., Sriram, V., Didenkulova, I., Fernandez, H., 2014. On the generation of tsunami in a large scale wave flume. In: Proc. 34th Int. Conf. on Coastal Engineering, Seoul, S. Korea.
- Sleath, J. F. A., 1987. Turbulent oscillatory flow over rough beds. *J. Fluid Mech.* 182, 369–409.

- Sumer, B. M., Jensen, P., Sørensen, L. B., Fredsøe, J., Liu, P. L.-F., Carstensen, S., 2010. Coherent structures in wave boundary layers. part 2. solitary motion. *J. Fluid Mech.* 646, 207–231.
- Sumer, B. M., Sen, M. B., Karagali, I., Ceren, B., Fredsøe, J., Sottile, M., Zilioli, L., Fuhrman, D. R., 2011. Flow and sediment transport induced by a plunging solitary wave. *J. Geophys. Res.* 116, C01008.
- Suntoyo, Tanaka, H., 2009. Numerical modelling of boundary layer flows for a solitary wave. *J. Hydro-environ. Research* 3, 129–137.
- Synolakis, C. E., 1986. The run-up of long waves. Ph.D. thesis, California Institute of Technology, Pasadena, California.
- Synolakis, C. E., 1987. The run-up of solitary waves. *J. Fluid Mech.* 185, 523–545.
- Tadepalli, S., Synolakis, C. E., 1994. The run-up of N-waves on sloping beaches. *Proc. R. Soc. Lond. A* 445, 99–112.
- Tanaka, H., Sana, A., Kawamura, I., Yamaji, H., 1999. Depth-limited oscillatory boundary layers on a rough bottom. *Coast. Eng. J.* 41, 85–105.
- Vittori, G., Blondeaux, P., 2008. Turbulent boundary layer under a solitary wave. *J. Fluid Mech.* 615, 433–443.
- Vittori, G., Blondeaux, P., 2011. Characteristics of the boundary layer at the bottom of a solitary wave. *Coastal Engineering* 58, 206–213.
- Wilcox, D. C., 2006. *Turbulence Modeling for CFD*, 3rd Edition. DCW Industries, Inc., La Canada, California.
- Yeh, H., Liu, P., Briggs, M., Synolakis, C. E., 1994. Propagation and amplification of tsunamis at coastal boundaries. *Nature* 372 (6504), 353–355.